Acta Metallurgica Sinica (English Letters) (2024) 37:1480–1490
https://doi.org/10.1007/s40195-024-01716-x

Experimental and DFT Investigations of AlNbTiVZr High Entropy Alloys with Excellent Mechanical Properties

Hongwei Yan[1,2,3] · Yong'an Zhang[1,2,3] · Wei Xiao[1,2,3] · Boyu Xue[1,2,3] · Rui Liu[1,2,3] · Xiwu Li[1,2,3] · Zhihui Li[1,2,3] · Baiqing Xiong[1,2,3]

Received: 15 January 2024 / Revised: 26 February 2024 / Accepted: 13 March 2024 / Published online: 28 June 2024

Abstract

This study investigated the microstructure and mechanical properties of AlNbTiVZr series high-entropy alloys (HEAs) through both experimental studies and density functional theory calculations. Significant improvements in the microstructures and mechanical properties were achieved for the AlNbTiVZr series HEAs by meticulously adjusting the alloy composition and employing homogenization heat treatment. Notably, the specimen designated as $Al_{0.5}NbTiVZr_{0.5}$ demonstrated excellent mechanical properties including a compressive yield strength of 1162 MPa and a compressive strength of 1783 MPa. After homogenization heat treatment at 1000 °C for 24 h, the $Al_{0.5}NbTiVZr_{0.5}$ alloy exhibits brittle-to-ductile transition. Further atomic-scale theoretical simulations reveal that the decrease of Al content intrinsically enhances the ductility of the alloys, thereby indicating that the mechanical properties of the AlNbTiVZr series HEAs were significantly influenced by the chemical composition. Additionally, specific atomic pair formations were observed to adversely affect the microstructure of the AlNbTiVZr series HEAs, particularly in terms of ductility. These findings provide valuable insights for the design and optimization of light weight HEAs, emphasizing the synergistic adjustment of alloy composition and heat treatment processes to achieve a balance between the strength and ductility.

Keywords High-entropy alloy · Microstructure · Mechanical properties · Density functional theory

1 Introduction

High entropy alloys (HEAs), defined as alloys containing four or more principal elements in equiatomic or nearequiatomic ratios [1], have emerged as a focal point of interest within the domain of materials science due to their exceptional performance. The unique structural characteristic of HEAs includes exceptional corrosion resistance, thermal resilience and mechanical performance stability. For instance, BCC-structured HEAs composed of refractory metals such as W, Zr, Hf, Cr, Ti, Ta, Nb and V have undergone extensive investigation for their remarkable mechanical properties and thermal stability across a spectrum of temperatures [2–6].

The microstructure and mechanical properties of HEAs are significantly dictated by the composition and proportion of alloying elements. Efforts to achieve weight reduction in HEAs have led to the incorporation of low-density elements, among which Al has been prevalently employed [7–11]. For example, the investigations conducted by Senkov et al. [12] have demonstrated that partial or total replacement of Hf/Cr with Al in HfNbTaTiZr and $CrMo_{0.5}NbTa_{0.5}TiZr$ alloys not only reduces the density of these alloys by at least 9%, but also enhances their hardness, yield strength by at least 12%, andhigh-temperature strength within the temperature range of 1073 K to 1473 K by more than 50%. Furthermore, research by Stepanov et al. [13–15] on AlNbTiVZr HEAs has elucidated that the increase of Al concentration correlates with an elevation in hardness. However, the phase

Available online at http://link.springer.com/journal/40195.

✉ Yong'an Zhang
zhangyongan@grinm.com

✉ Baiqing Xiong
xiongbq@grinm.com

[1] State Key Laboratory of Nonferrous Metals and Processes, China GRINM Group Co., Ltd., Beijing 100088, China

[2] GRIMAT Engineering Institute Co., Ltd., Beijing 101407, China

[3] General Research Institute for Nonferrous Metals, Beijing 100088, China

composition of the HEA becomes more complex with the incorporation of Al element, encompassing not only the BCC matrix but also integrating C14 Laves phase and Zr_2Al particles. This alteration in microstructure caused significant deterioration of ductility in refractory HEAs with elevated Al content. Homogenization treatment have been identified as a viable strategy to counteract this adverse effect, thus enhancing the overall properties. Chen et al. [16] found that the compressive yield strength of AlNbTiZr HEA increased to 1579 MPa after homogenization, and the ultimate compressive strength, fracture strain improved by 308 MPa and 9.2%, respectively, compared to as-cast HEA. Additionally, homogenization treatments performed by Yurchenko et al. [17] on the $Al_{20}Cr_{10}Nb_{15}Ti_{20}V_{25}Zr_{10}$ alloy at 1200 °C resulted in an approximate 50% increase in yield strength while retaining similar ductility.

The application of density functional theory (DFT) calculations has been recognized as an effective way for the optimization and conceptualization of novel HEAs [18–20]. The work of Jeong et al. [21] exemplifies this approach combined with DFT calculations to investigate 40 single-phase solid-solution lightweight HEAs with BCC structure. Their comprehensive analysis reveals that the valence electron concentration plays a crucial role in determining the elastic modulus. This underscores the significance of electronic structure in influencing the mechanical behavior of HEAs. As for the NbVTiZr series HEAs, Qiu et al.[22] elucidated the mechanism of strengthening by adding Al element. This enhancement can be primarily attributed to the strong angular characteristic bonds formed between the introduced Al atoms and the existing transition metal atoms.

Thus, a synergistic approach combining both computational methods and experimental techniques is promising to yield HEAs with superior mechanical properties, thereby broadening the applicability of HEAs in advanced engineering and technological applications.

So far, the reported AlNbTiVZr series HEAs have exhibited commendable strength, but their ductility is less than desirable. This study employs a synergistic approach that combines theoretical calculations and experimental preparation to investigate the influence of elemental ratio and heat treatment processes on the microstructure and mechanical properties of AlNbTiVZr series HEAs. This integrative approach provides a strategy for optimizing the performance in the design of HEAs, with the goal of developing novel AlNbTiVZr HEAs that exhibit comprehensive high ductility and excellent strength.

2 Materials and Methods

2.1 Experimental Procedures

In this study, we prepared as-cast button-like HEAs ingots using raw metal particles with purity exceeding 99.99% by vacuum arc melting (VAM) process. These samples were designated as AlNbTiVZr (Al-Zr) and $Al_{0.5}NbTiVZr_{0.5}$ ($Al_{0.5}$-$Zr_{0.5}$) respectively, and the mass was about 200 g each ingot. The compositions of these ingots are listed in Table 1. To ensure the homogenization, the samples were flipped seven times within the vacuum furnace chamber. Subsequently, cubic specimens which were 10 mm in length were electric discharge wire cut from the central part of the ingot, and then ground mechanically using the SiC paper ranging from 240# to 5000#, followed by a 20-min polishing with diamond paste.

To eliminate element segregation induced during the preparation of these HEAs samples, these cubic specimens were homogenized at 800 °C and 1000 °C for 24 h. Prior to homogenization, the specimens were sealed in a quartz tube along with pure titanium pellets to prevent oxidation and a near vacuum environment were maintained with an internal pressure of 10^{-2} MPa. After homogenization, the quartz tube samples were air-cooled to room temperature. The microstructure evolution and element distribution of the as-cast and homogenized specimens were observed by a scanning electron microscope (SEM, JEOL JSM 7001F) equipped with an X-ray energy spectrometer. Compression tests were performed on cylindrical specimens with the diameter of 6 mm and height of 9 mm using the universal testing machine (MTS 858, USA) at a compression speed of 1 mm·min^{-1} until the height reduction exceeded 40% according to ASTM D695 standards.

Table 1 Compositions of the alloys (at.%)

Alloys		Al	Ti	V	Zr	Nb
AlNbTiVZr	Nominal	20	20	20	20	20
	800 °C	19	25	16	18	22
	1000 °C	20	20	20	20	20
$Al_{0.5}$Nb TiV$Zr_{0.5}$	Nominal	12.5	25	25	12.5	25
	800 °C	12	29	28	12	19
	1000 °C	12	25	25	13	25

2.2 Calculation Details

All calculations were carried out using the density functional theory (DFT) framework as implemented in the Vienna ab initio simulation package (VASP) [23–25]. The electron–ion interactions were described using the projector augmented wave (PAW) method [26]. The exchange and correlation effects among electrons were treated within the generalized gradient approximation (GGA) [27] in the Perdew-Burke-Ernzerhof (PBE) form [28]. A cutoff energy of 500 eV was chosen for convergence. For all 128-atom AlNbTiVZr HEAs supercells, a 5×5×5 k-point gird automatically generated with a Gamma-centered scheme was adopted for all cell optimizations until the total energy and force of the system were converged to an accuracy of 10^{-5} eV and 0.01 eV/Å, respectively.

In this work, considering the random distribution of alloying atoms, the HEAs supercells were constructed with 128 atoms (4×4×4 unit cells) in a BCC lattice using the special quasi-random structure (SQS) approach [29]. The method utilizes the mcsqs code within the Alloy-Theoretic Automated Toolkit (ATAT) [30] to simulate random solid solutions. Figure 1 shows the SQS supercell of $Al_{26}Nb_{26}Ti_{26}V_{26}Zr_{24}$, which approximately matches the atomic composition of the AlNbTiVZr HEA. Additionally, Monte Carlo (MC) method combined with DFT calculations was employed to study the effect of chemical short-range order (CSRO) on the property of these HEAs as a comparison. The optimized SQS structure was used as the initial starting point for MC simulations. The simulations were conducted at a temperature of 600 K. To enhance the computational efficiency, a relatively low precision with a cutoff energy of 350 eV for plane waves and a 3×3×3 k-point gird for Brillouin zone integration was utilized to obtain different structural models with varying degrees of CSRO. The CSRO value can be qualified by Warren-Cowley SRO parameters [31]:

$$\alpha_{ij}^{v} = 1 - \frac{p_{ij}^{v}}{c_j}. \tag{1}$$

where p_{ij}^{v} denotes the probability of finding atomic species j around an atom of type i in the v's neighboring shell and c_j is the atomic concentration of type j. The SRO $\alpha = 0.0$ indicates that the system is a randomly disordered solution. Positive values show a tendency to decrease the number of ij atom pairs, while negative values indicate the opposite tendency. To evaluate the CSRO, the nearest-neighbor shell in BCC structure was considered, and the sum of CSRO was defined as $\sum \left|\alpha_{ij}^{v}\right|$.

For the HEA systems, the density derived electrostatic and chemical (DDEC6) charge partitioning method can be used to determine atomic binding characteristics [32,33]. Mechanical properties can be derived by the energy-strain method implemented in the VASPKIT package [34]. The three independent elastic constants C_{11}, C_{12} and C_{44} are represented in the form of an elastic stiffness tensor matrix for cubic structures:

$$C_{ij}^{\text{cubic}} = \begin{pmatrix} C_{11} & C_{12} & C_{12} & & & \\ C_{12} & C_{11} & C_{12} & & & \\ C_{12} & C_{12} & C_{11} & & & \\ & & & C_{44} & & \\ & & & & C_{44} & \\ & & & & & C_{44} \end{pmatrix}. \tag{2}$$

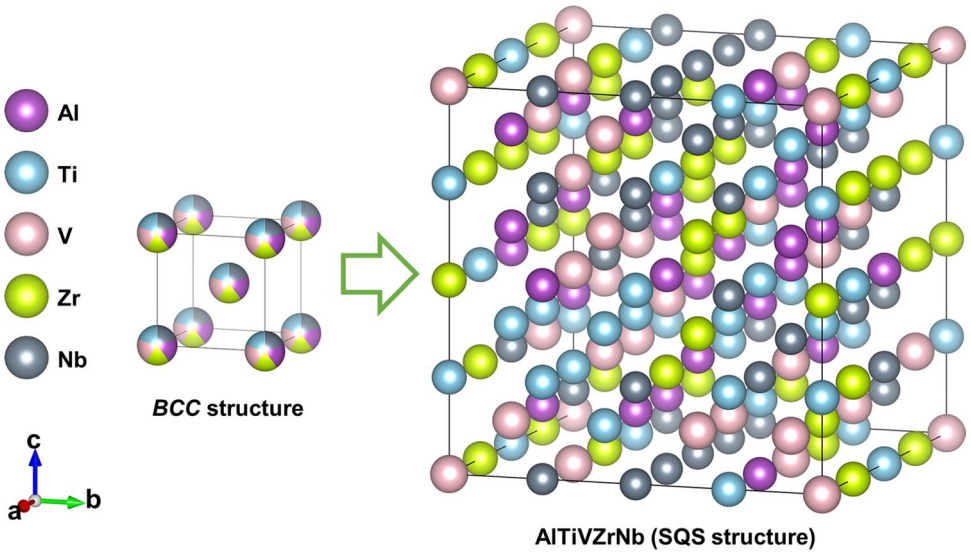

Fig. 1 Crystal models of $Al_{26}Nb_{26}Ti_{26}V_{26}Zr_{24}$

3 Results and Discussion

3.1 Microstructure and Mechanical Properties of the AlNbTiVZr Series HEAs

Figure 2 illustrates the microstructural evolution of the as-cast and homogenized specimens. It is discernible that the homogenization process significantly influences the microstructure of the AlNbTiVZr series HEAs, especially for the specimen homogenized at a higher temperature. For the specimens designated as Al-Zr and $Al_{0.5}$-$Zr_{0.5}$ subjected to homogenization at 1000 °C for 24 h (as depicted in Fig. 2a3 and b3), no obvious contrast variation is observed. This uniformity in contrast is suggestive of a comprehensive intermixing of the five principal elements, thereby facilitating the realization of the high-entropy effect by forming a highly randomized atomic arrangement and suggesting superior mechanical properties after 1000 °C/24 h homogenization. According to our previous study [35], it is identified that the dark regions and bright regions observed in the as-cast sample are indicative of the BCC structure phase and the ZrAlV intermetallic, respectively. The bright ZrAlV phases are prone to wrap the BCC structures and divide them into block morphology. As for the $Al_{0.5}$-$Zr_{0.5}$ specimen, due to low Al and Zr content, the BCC structures connect and coarsen while the brittle intermetallics discontinuously distributed. The decreased amount of intermetallics indicates an improvement in mechanical properties compared to the as-cast Al-Zr specimen. Following the homogenization at 800 °C for 24 h (as depicted in Fig. 2a2 and b2), a diminution in the size of the dark BCC phases is observed. Additionally, an increased prevalence of diminutive, discrete block-like bright phases is noted, interspersed among the BCC phase and surrounding the bright ZrAlV intermetallics. Specifically, in the case of the $Al_{0.5}$-$Zr_{0.5}$ specimen, the BCC structure phase is observed to assume a position of dominance as shown in Fig. 2b2. The previously coarse ZrAlV intermetallics undergo transformation into slender, elongated lens-shaped phases after the homogenization treatment.

To elucidate the segregation behavior of different elements within HEAs, the energy dispersive spectroscopy (EDS) elemental mapping of the specimens after homogenization is depicted in Fig. 3. The analysis derived from EDS is shown in Table 1. In the case of the Al-Zr specimen, even after homogenization at 1000 °C, the distribution of Ti and Zr remains relatively notably heterogeneous. The bright phases wrapped in BCC structure phases exhibit an enrichment of Zr and a corresponding depletion of Ti. The homogenization treatment did not eliminate the element segregation completely, possibly attributable to the Al-Zr element pair which processes the most negative binary mixing enthalpy value among the constituents of the AlNbTiVZr series HEAs. In contrast, the elemental segregation of the $Al_{0.5}$-$Zr_{0.5}$ specimen is significantly improved after homogenization at 1000 °C for 24 h (as depicted in Fig. 3b2). The

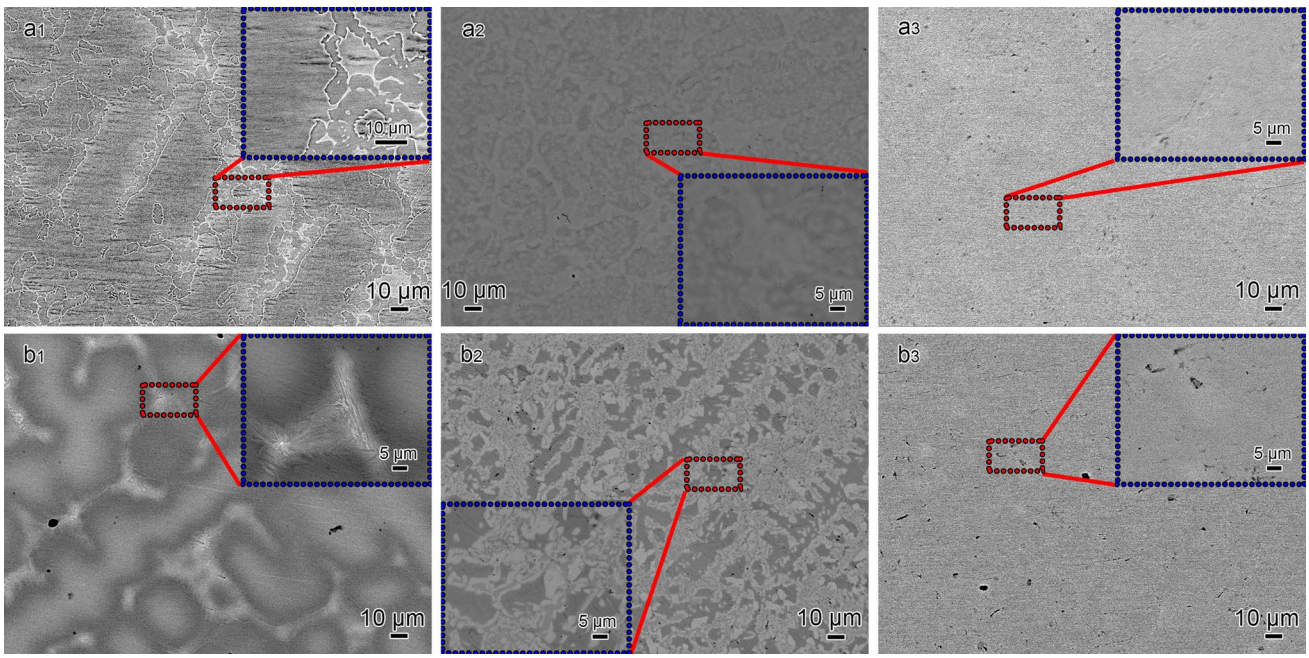

Fig. 2 SEM images of the microstructure of the as-cast and annealed HEAs specimens. $\mathbf{a_1}$ as-cast Al-Zr; $\mathbf{a_2}$ Al-Zr annealing of 800 °C/24 h; $\mathbf{a_3}$ Al-Zr of annealing 1000 °C/24 h; $\mathbf{b_1}$ as-cast $Al_{0.5}$-$Zr_{0.5}$ $\mathbf{b_2}$ $Al_{0.5}$-$Zr_{0.5}$ annealing of 800 °C/24 h, $\mathbf{b_3}$ $Al_{0.5}$-$Zr_{0.5}$ annealing of 1000 °C/24 h

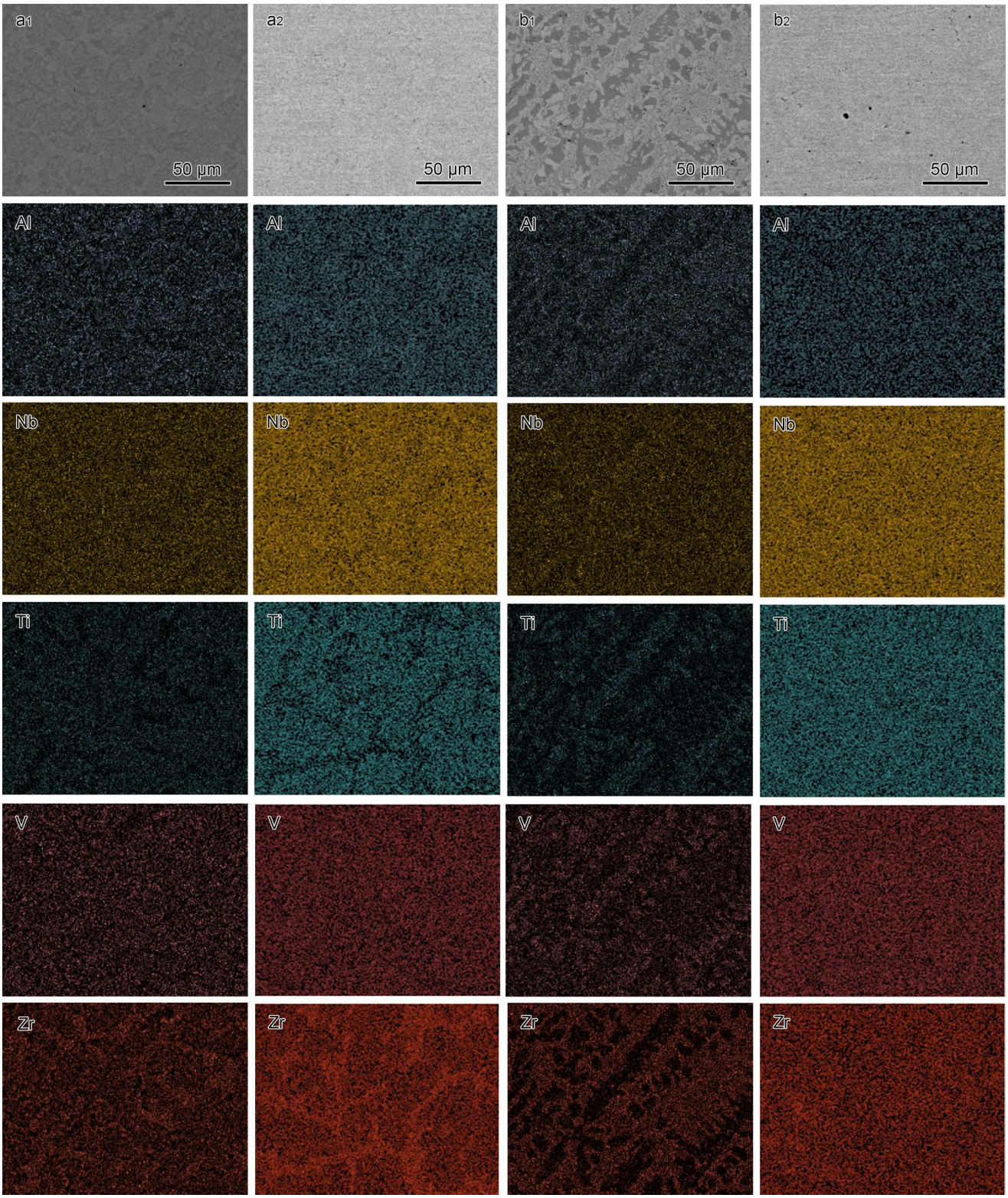

Fig. 3 Element distribution in the two HEAs after annealing: $\mathbf{a_1}$ Al-Zr at 800 °C; $\mathbf{a_2}$ Al-Zr at 1000 °C; $\mathbf{b_1}$ $Al_{0.5}$-$Zr_{0.5}$ at 800 °C; $\mathbf{b_2}$ $Al_{0.5}$-$Zr_{0.5}$ at 1000 °C

distribution of each principal element appears significantly more homogeneous, and the elemental composition closely aligns with the nominal composition, as detailed in Table 1. Furthermore, as demonstrated in Table 1, the concentrations of Al and Zr elements remain remarkably consistent throughout the homogenization treatment process for both specimens. This consistency suggests an inherent tendency for these elements to form a stable phase within the AlNbTiVZr series HEAs.

Figure 4a delineates the engineering compression stress–strain curves for both as-cast and homogenized specimens with varying compositions. For the specimen homogenized at 800 °C, the presence of phase with inherent brittleness near the boundaries of the BCC structure leads to the initiation of cracks during the deformation process, which results in premature fracture even in the elastic deformation stage. Consequently, the engineering compression curve of this specimen is omitted from presentation. A noteworthy observation is the manifestation of a brittle-ductile transition in the $Al_{0.5}$-$Zr_{0.5}$ specimen subsequent to homogenization at 1000 °C for 24 h. This specimen demonstrates an engineering strain exceeding 40%, with an ascending trajectory attributable to the equitable distribution of principal elements. The relevant mechanical properties are also listed in Fig. 4b for comparison. After homogenization, the Al-Zr specimen exhibits enhancements in yield strength ($\sigma_{0.2}$) and ultimate compression strength (σ_p) to 1344 MPa and 1471 MPa, respectively, marking significant increments of 12.28% and 16.19%. However, the homogenized Al-Zr specimen shows a marginal reduction in fracture strain alongside a constricted yield stage, which suggests an incomplete elimination of Al and Zr segregation after homogenization at 1000 °C. This segregation engenders the formation of intermetallic compounds, encapsulating other phases within the alloys. Further homogenization at higher temperatures might be necessary to provide sufficient kinetic energy for atomic diffusion within the equiatomic HEA to eliminate the segregation effect. Contrastingly, when the concentration of Al and Zr elements is reduced, the mechanical properties of the as-cast $Al_{0.5}$-$Zr_{0.5}$ specimen were significantly improved, with $\sigma_{0.2}$ and σ_p reaching 1162 and 1783 MPa, respectively, in conjunction with a substantial improvement in fracture strain to 28.8%. This elucidates that, in addition to the positive influence of the heat treatment process on the mechanical properties of the AlNbTiVZr HEAs, a reduction in the Al and Zr content also contributes to an enhancement in both strength and ductility of the AlNbTiVZr series HEAs.

3.2 Atomic Mechanism Analysis of HEAs

DFT calculations are commonly used to predict the thermodynamic, structural, and elastic characteristics of alloys. This computational method facilitates in-depth insights into the structure–property relationships of alloys and provides theoretical guidance for alloy design. By utilizing this method, we compared the differences in performance between different compositions and chemical ordered structures, including formation energies, electronic structures, and mechanical properties.

3.2.1 Chemical Composition Effect

To evaluate the thermodynamic stability of the AlNbTiVZr series HEAs, the formation energy at 0 K can be derived by the equation:

$$E_{\text{form}} = \frac{E_{\text{tot}} - \sum N_i E_i^{\text{bulk}}}{128}. \tag{3}$$

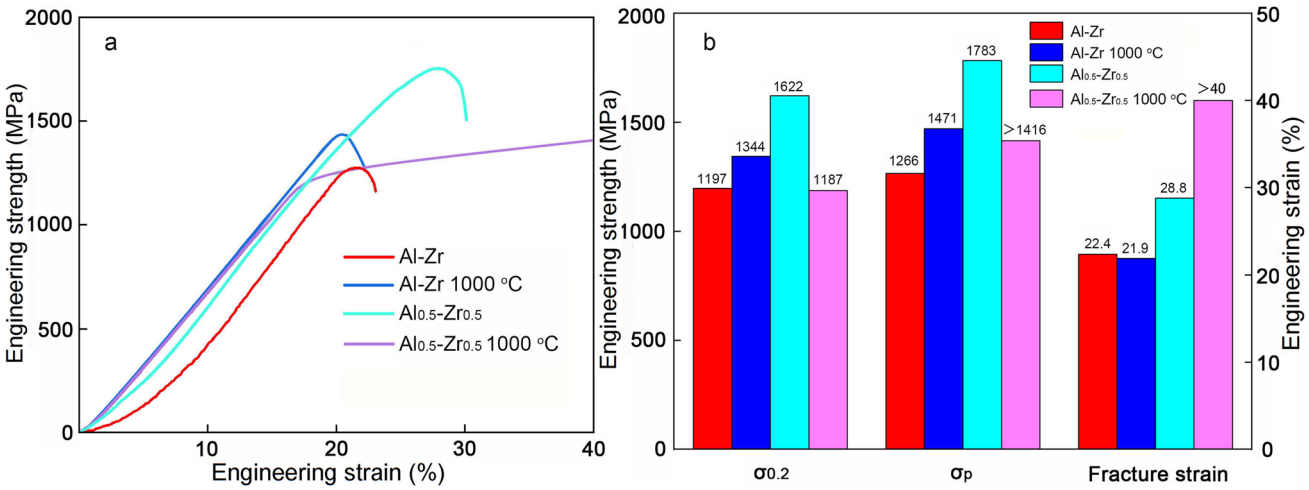

Fig. 4 **a** Engineering compression stress–strain curves, **b** relevant mechanical properties

where E_{tot} represents the total energy of the AlNbTiVZr HEA system, N_i represents the number of atoms of different alloying elements, and E_i^{bulk} represents their corresponding energy values in ground states per atom, as listed in Table 2 [12]. The formation energies of the $Al_{26}Nb_{26}Ti_{26}V_{26}Zr_{24}$ and $Al_{16}Nb_{32}Ti_{32}V_{32}Zr_{16}$ structures obtained through SQS modeling are -0.04 and 0 eV/atom, respectively, as is shown in Table 3. The calculated formation energy of HEAs is relatively low, approaching 0 eV/atom, which signifies the possibility of experimentally obtaining the discussed alloys. Additionally, the predicted valence electron concentration (VEC) values for both alloys are less than 6.87 as shown in Table 3, suggesting the formation of BCC structure, corroborating the theoretical framework presented in existing literature [36]. Furthermore, the decreasing trend of the formation energy with the increase in Al concentration is consistent with the findings by Qiu et al. [22], indicating that the incorporation of Al enhances the thermodynamic stability of the alloy. The calculated lattice constant for the structure of $Al_{16}Nb_{32}Ti_{32}V_{32}Zr_{16}$ and $Al_{26}Nb_{32}Ti_{26}V_{26}Zr_{24}$ structures are 0.324 nm and 0.326 nm, respectively. These calculated values align closely with the values reported by Vishwanadh et al. (0.325 nm) [37] and Qiu et al. (0.326 nm) [22], thereby validating the robustness and reliability of the DFT method used in this study.

To analyze the strengthening mechanisms accurately, we calculated the elastic constants of the AlNbTiVZr series HEAs. Based on these elastic constants from DFT calculations, the shear modulus (G) and bulk modulus (B) can be calculated using the Voigt-Reuss-Hill (VRH) method [38–43]. The VRH method provides a precise theoretical evaluation for polycrystalline materials by taking the average between the lower Voigt and the upper Hill boundaries, which can be expressed as:

$$\begin{cases} B = \frac{1}{2}(B_V + B_R) = \frac{1}{2}\left[\frac{C_{11}+2C_{12}}{3} + \frac{1}{3(S_{11}+2S_{12})}\right] \\ G = \frac{1}{2}(G_V + G_R) = \frac{1}{2}\left[\frac{(C_{11}-2C_{12})+3C_{44}}{5} + \frac{5}{4(S_{11}-S_{12})+3S_{44}}\right] \end{cases} \quad (4)$$

where S_{ij} is the compliance tensor, which is the inverse of the stiffness matrix C_{ij}. The Young's modulus E and Poisson's ratio ν can be obtained from these values:

$$\begin{cases} E = \frac{9BG}{3B+G} \\ \nu = \frac{3B-2G}{2(3B+G)} \end{cases} \quad (5)$$

Table 3 provides the calculated elastic constants of the $Al_{26}Nb_{26}Ti_{26}V_{26}Zr_{24}$ and $Al_{16}Nb_{32}Ti_{32}V_{32}Zr_{16}$ structures, satisfying the Born stability criteria for cubic crystals, specifically: C_{11}-$C_{12}>0$, $C_{11}+2C_{12}>0$, $C_{11}>0$ and $C_{12}>0$. It suggests that both structures are mechanically stable. An analytical review of the results for the $Al_{26}Nb_{26}Ti_{26}V_{26}Zr_{24}$ structure shows that the mechanical properties B, E, and G are quantified as 122.3 GPa, 85.5 GPa, and 30.9 GPa, respectively. For the $Al_{16}Nb_{32}Ti_{32}V_{32}Zr_{16}$ structure, the bulk modulus is calculated to be 127.7 GPa, which is close to that of the $Al_{26}Nb_{26}Ti_{26}V_{26}Zr_{24}$ structure. However, the decrease in C_{44} has led to a diminution in both E to 73.4 GPa and G to 26.2 GPa. The change in composition principally affects the E and G values of the AlNbTiVZr HEAs, resulting in a large increase of the B/G ratio to 4.9. Such an increase significantly enhances the ductility of the $Al_{16}Nb_{32}Ti_{32}V_{32}Zr_{16}$

Table 2 Atomic radius, Pauling electronegativity, VEC, density, crystal structure, and ground state energy per atom for alloying elements [12,36]

	Atomic No	Atomic radius (Å)	Pauling electronegativity	VEC	ρ (g·cm^{-3})	Crystal structure (RT)	E_i^{bulk}(eV·atom^{-1})
Al	13	1.43	1.61	3	2.7	FCC	−3.75
Ti	22	1.46; 1.47	1.54	4	4.51	HCP	−7.76
V	23	1.32; 1.34	1.63	5	6.00; 6.11	BCC	−8.94
Zr	40	1.6	1.55; 1.33	4	6.51; 6.52	HCP	−8.52
Nb	41	1.43; 1.46	1.6	5	8.57	BCC	−10.21

Table 3 Calculated lattice constant, VEC, formation energy, and elastic constants of different HEAs

Alloys	Source	α (nm)	VEC	E_{form} (eV·atom^{-1})	C_{11}	C_{12}	C_{44}	B	E	G	ν	B/G
AlNbTiVZr	$Al_{26}Nb_{26}Ti_{26}V_{26}Zr_{24}$ (SQS)	0.326 0.325[37] 0.326[[22]]	4.20	−0.04	150.3	108.3	40.0	122.3	85.5	30.9	0.393	3.96
	$Al_{26}Nb_{26}Ti_{26}V_{26}Zr_{24}$ (MC)	0.326	4.20	−0.10	158.5	106.8	46.1	124.0	99.9	36.6	0.366	3.39
$Al_{0.5}NbTiVZr_{0.5}$	$Al_{16}Nb_{32}Ti_{32}V_{32}Zr_{16}$ (SQS)	0.324	4.38	0.00	150.7	116.3	34.6	127.7	73.4	26.2	0.404	4.88

structure alloy compared to the $Al_{26}Nb_{26}Ti_{26}V_{26}Zr_{24}$ structure. Invoking Pugh's criterion [44], which posits that a polycrystalline material is deemed ductile if the ratio of *B*/*G* exceeds 1.75, it becomes evident that a reduction in the concentrations of Al and Zr exerts a negligible effect on the *B* value and slightly decreases the values of *E* and *G*. This alteration effectively enhances the ductility of the AlNbTiVZr series HEAs. These simulation results well explain the enhanced plasticity observed in the $Al_{0.5}$-$Zr_{0.5}$ specimen during experimental investigations.

To elucidate the compositional effect on the alloy performance at the atomic scale, we conducted a comparative analysis and examination of the bonding characteristics of these two structures as depicted in Fig. 5. Within this quinary alloy system, the bond orders of atomic pairs involving Nb, such as Nb-Nb, Nb-V, and Nb-Zr bonds, are relatively high, typically exceeding 0.3. In contrast, the chemical bonds that incorporate Al, such as Al-Al, Al-Ti, Al-Zr, and Al-V bonds, exhibit relatively weak bond orders, ranging from 0.20 to 0.25. Figure 6a presents the density of states (DOS) for the $Al_{26}Nb_{26}Ti_{26}V_{26}Zr_{24}$ alloy in a SQS structure. The total DOS at the Fermi level (E_F) is non-zero, indicating a distinct metallic behavior for this system. The electronic states near the E_F predominantly comprise Al-*p* orbitals and *d* orbitals of other transition metals (Ti, V, Zr and Nb). Notably, the *d* electrons of all transition metals are strongly localized, causing them to show distinct shape features in the DOS near the E_F. Among these transition metals, the Nb-*d* and V-*d* orbitals exhibit remarkable similarity, positioned to the left of the E_F, whereas for Zr and Ti atoms, their *d* orbital peaks align precisely with the E_F. Furthermore, upon simultaneously reducing the contents of Al and Zr, the system is predominantly occupied by the bonds related to Nb, Ti and V, while the bonds associated with Al and Zr are reduced by approximately half. Consequently, the alterations in bonding characteristics caused by the composition differences could significantly reduce the formation of intermetallic related to Al-Zr, thereby affecting the mechanical properties of the AlNbTiVZr series HEAs.

3.2.2 CSRO Effect

In contrast to pure metals and conventional alloys, HEAs samples often exhibit local chemical inhomogeneities often occur in actual HEAs samples, which may also affect the strength and ductility of the alloy. To address this issue, we employed a DFT-based Monte Carlo simulation to explore the CSRO effect in the $Al_{26}Nb_{26}Ti_{26}V_{26}Zr_{24}$ refractory HEA. The MC structure refers to the preliminary form or stage of local chemical ordering. The final state is obtained through approximately 2000 steps of MC simulation when the potential energy stabilizes, and the cumulative CSRO value increases from 1.19 in the SQS structure to 4.69. As listed in Table 3, the formation energy of the alloy in its final CSRO configuration drops to − 0.10 eV/atom from its initial random state, suggesting that the energy difference

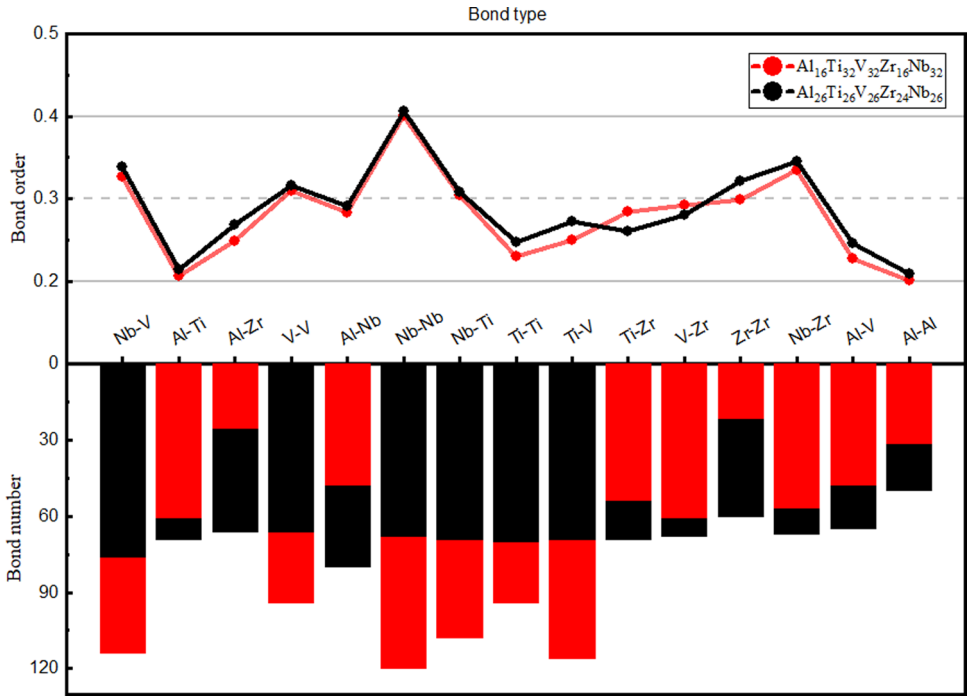

Fig. 5 Comparison of the bond order and bond number for the $Al_{26}Nb_{26}Ti_{26}V_{26}Zr_{24}$ and $Al_{16}Nb_{32}Ti_{32}V_{32}Zr_{16}$ structures

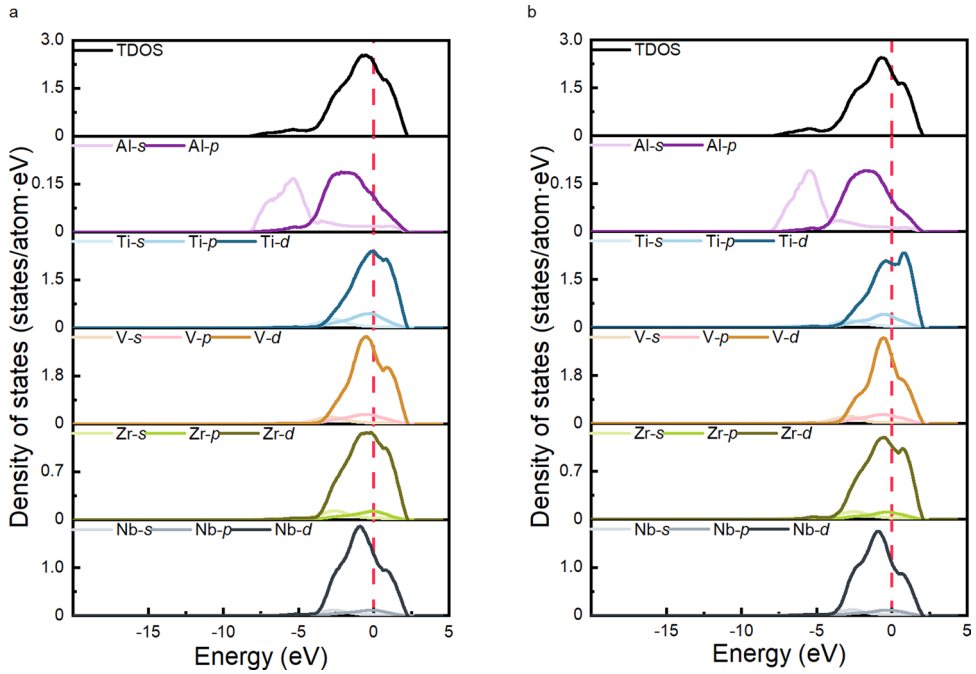

Fig. 6 Calculated density of states (DOS) of $Al_{26}Nb_{26}Ti_{26}V_{26}Zr_{24}$ with both **a** SQS, **b** MC structures. The Fermi energies are set to 0 eV, marked by vertical dashed lines

after structural optimization is attributable to the alterations in atomic arrangement induced by the CSRO effect. As illustrated in the Fig. 7, in the MC structure, the CSRO (charge density difference) values for Al-Ti and Al-Zr bonds are significantly negative (below -0.6), indicating a strong tendency toward the formation of chemically favorable atom pairs in the alloy. Conversely, the CSRO values for Al-Al, Ti–Ti, and Ti-Zr bonds are positive (greater than 0.4), signifying a decrease in the number of these atom pairs. The comparative analysis of bonding characteristics between the two structures reveals that both the number and the order of Al-Ti and Al-Zr bonds have increased after MC simulation, as is shown in Fig. 8. According to existing literature [12], the enthalpy of formation for Al-Zr intermetallic phase ranges from − 43.7 to − 41.4 kJ/mol, whereas for Al-Ti intermetallic phase, it is spans from − 30 to − 20 kJ/mol. Therefore, in high-aluminum content refractory HEAs, the formation of Al-Zr intermetallics are thermodynamically more favorable. The formation of these Al-Zr atom pairs could provide a foundation for subsequent compound formation.

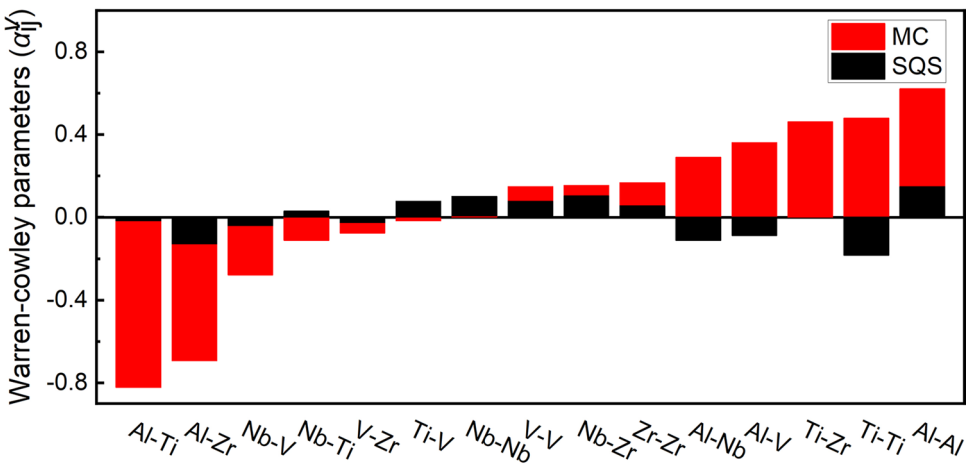

Fig. 7 α_{ij}^{v} of different pairs for the first nearest-neighbor shell of the SQS and MC structures of $Al_{26}Nb_{26}Ti_{26}V_{26}Zr_{24}$

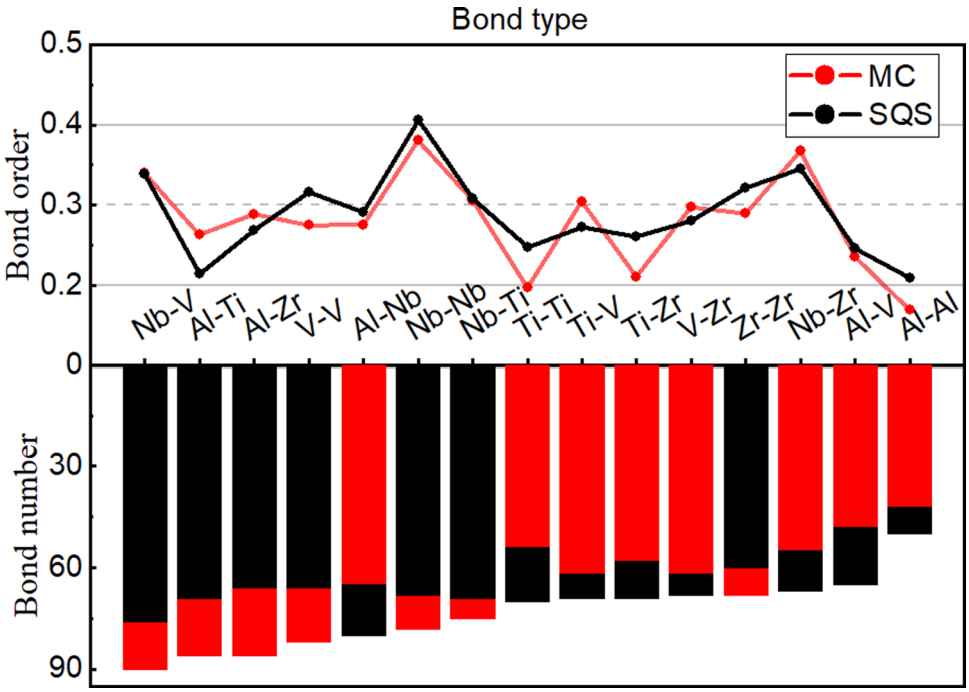

Fig. 8 Comparison of the bond order and bond number of the SQS and MC structures of $Al_{26}Nb_{26}Ti_{26}V_{26}Zr_{24}$

Furthermore, as shown in Table 2, among the constituent elements, Zr exhibits significant atomic size differences [45], which is generally unfavorable for the formation of disordered solid solutions, thus explaining the segregation behavior of Al-Zr elements in the AlNbTiVZr series HEAs specimens as depicted in Figs. 2 and 3. Besides, as is shown in Fig. 8, the bond strengths of Al-Al, Zr-Zr, Ti-Zr, Ti–Ti and V-V pairs are weakened in the MC structure.

The calculated mechanical properties of the MC structure show an obvious decrease in E and G, as listed in Table 3, resulting a lower B/G value (3.4) and Poisson's ratio v (0.37). This indicates that the CSRO effect diminishes the ductility of the alloy, primarily due to the change in the number and strength of various atom pairs. A comparison of elastic constants between the MC and SQS structures reveals a significant variance in the C_{44} coefficient, approximately 15%, as listed in Table 3. C_{44} describes the shear resistance at the (100) crystal plane along the [001] direction [21,39,40], and a higher value indicates greater corresponding resistance. Thus, the elastic constants E and G demonstrate heightened sensitivity to the CSRO effect. In addition, DOS analysis (as shown in Fig. 6) shows that the MC structure displays two peaks located on both sides of the Fermi level for Ti and Zr elements compared to the SQS structure, resulting in the formation of a pseudo band gap. This signifies that the bond strength of the relevant atomic pairs has also changed. In summary, the CSRO effect profoundly affects the mechanical properties of the AlNbTiVZr series HEAs, contributing to the observed reduction in ductility.

4 Conclusions

In this study, the influence of alloy composition and heat treatment processes on the microstructure and mechanical properties of AlNbTiVZr series HEAs has been investigated through a combination of experimental approaches and DFT calculations. Our research findings are summarized as follows:

1. The microstructure and mechanical properties of AlNbTiVZr HEAs were significantly improved through reduction of Al and Zr composition. Compared to the Al-Zr specimen, the as-cast $Al_{0.5}$-$Zr_{0.5}$ specimen exhibited superior mechanical properties, with a yield strength and an ultimate compression strength of 1162 and 1783 MPa, respectively.
2. After homogenization treatment at 1000 °C for 24 h, the $Al_{0.5}$-$Zr_{0.5}$ specimen exhibited a brittle-to-ductile transition, maintaining its structural integrity without fracturing even when subjected to the compression strain exceeding 40%.
3. Atomic-scale theoretical simulations provided profound insights into the influence of alloy composition and CSRO on the performance of HEAs. It has been elucidated that reducing the content of Al and Zr is beneficial for enhancing the ductility of the HEAs. Furthermore, the CSRO effect promotes the formation of certain specific atomic pairs, thereby exerting a negative influence on the microstructure of AlNbTiVZr serise HEAs, ultimately compromising the mechanical properties of the HEAs, particularly their ductility.

Acknowledgements This work was financially supported by the Innovation Fund Project of GRINM (No. 5232210).

Declarations

Conflict of interest The authors declare that there are no conflicts of interest to disclose.

References

[1] B. S. Murty, J.W. Yeh, S. Ranganathan, P. Bhattacharjee, *High-entropy alloys* (Elsevier, 2019), pp. 23–30
[2] J.W. Yeh, S.K. Chen, S.J. Lin, J.Y. Gan, T.S. Chin, T.T. Shun, C.H. Tsau, S.Y. Chang, Adv. Eng. Mater. **6**, 299 (2004)
[3] Z. Guo, X. Shen, F. Liu, J. Guan, Y. Zhang, F. Dong, Y. Wang, X. Yuan, B. Wang, L. Luo, Y. Su, J. Cheng, J. Alloy. Compd. **960**, 170739 (2023)
[4] Q. Wei, A. Zhang, J. Han, B. Xin, B. Su, X. Wang, J. Meng, Mater. Sci. Eng. A **857**, 144035 (2022)
[5] H. Zhang, J. Cai, J. Geng, X. Sun, Y. Zhao, X. Guo, D. Li, Int. J. Refract. Met. H. **112**, 106163 (2023)
[6] W. Huang, X. Wang, J. Qiao, Y. Wu, J. Alloy. Compd. **914**, 165187 (2022)
[7] C.J. Tong, M.R. Chen, J.W. Yeh, S.J. Lin, S.K. Chen, T.T. Shun, S.Y. Chang, Metal. Mater. Trans. A **36**, 1263 (2005)
[8] H. Xu, M. Zhang, G. Zhang, G. Li, G. Li, Mater. Charact. **207**, 113516 (2024)
[9] B. Kang, J. Lee, H.J. Ryu, S.H. Hong, J. Alloy. Compd. **767**, 1012 (2018)
[10] P. Chakraborty, A. Sarkar, K. Ali, J. Jha, N. Jothilakshmi, A. Arya, R. Tewari, Int. J. Refract. Met. H. **113**, 106222 (2023)
[11] M. Li, Q. Chen, X. Cui, X. Peng, G. Huang, J. Alloy. Compd. **857**, 158278 (2021)
[12] O.N. Senkov, S.V. Senkova, C. Woodward, Acta Mater. **68**, 214 (2014)
[13] N.D. Stepanov, D.G. Shaysultanov, G.A. Salishchev, M.A. Tikhonovsky, Mater. Lett. **142**, 153 (2015)
[14] N.D. Stepanov, N.Y. Yurchenko, D.G. Shaysultanov, G.A. Salishchev, M.A. Tikhonovsky, Mater. Sci. Technol. **31**, 1184 (2015)
[15] N.D. Stepanov, N.Y. Yurchenko, D.V. Skibin, M.A. Tikhonovsky, G.A. Salishchev, J. Alloy. Compd. **652**, 266 (2015)
[16] W. Chen, Q.H. Tang, H. Wang, Y.C. Xie, X.H. Yan, P.Q. Dai, Mater. Sci. Technol. **34**, 1309 (2018)
[17] N. Yurchenko, E. Panina, M. Tikhonovsky, G. Salishchev, S. Zherebtsov, N. Stepanov, Mater. Lett. **264**, 127372 (2020)
[18] S. Yang, G. Liu, Y. Zhong, J. Alloy. Compd. **916**, 165477 (2022)
[19] V. Sorkin, Z.G. Yu, S. Chen, T.L. Tan, Z.H. Aitken, Y.W. Zhang, Sci. Rep. **12**, 11894 (2022)
[20] M. Rittiruam, J. Noppakhun, S. Setasuban, N. Aumnongpho, A. Sriwattana, S. Boonchuay, T. Saelee, C. Wangphon, A. Ektarawong, P. Chammingkwan, T. Taniike, S. Praserthdam, P. Praserthdam, Sci. Rep. **12**, 16653 (2022)
[21] I.S. Jeong, J.H. Lee, Mater. Des. **227**, 111709 (2023)
[22] S. Qiu, N. Miao, J. Zhou, Z. Guo, Z. Sun, Intermetallics **92**, 7 (2018)
[23] G. Kresse, J. Furthmüller, Phys. Rev. B **54**, 11169 (1996)
[24] G. Kresse, J. Furthmüller, Comput. Mater. Sci. **6**, 15 (1996)
[25] G. Kresse, D. Joubert, Phys. Rev. B **59**, 1758 (1999)
[26] P.E. Blöchl, Phys. Rev. B **50**, 17953 (1994)
[27] J.P. Perdew, J.A. Chevary, S.H. Vosko, K.A. Jackson, M.R. Pederson, D.J. Singh, C. Fiolhais, Phys. Rev. B **46**, 6671 (1992)
[28] J.P. Perdew, K. Burke, M. Ernzerhof, Phys. Rev. Lett. **77**, 3865 (1996)
[29] C. Jiang, Acta Mater. **57**, 4716 (2009)
[30] A. van de Walle, M. Asta, G. Ceder, Calphad **26**, 539 (2002)
[31] J.M. Cowley, Phys. Rev. **77**, 669 (1950)
[32] T.A. Manz, RSC Adv. **7**, 45552 (2017)
[33] N.G. Limas, T.A. Manz, RSC Adv. **8**, 2678 (2018)
[34] V. Wang, N. Xu, J.C. Liu, G. Tang, W.T. Geng, Comput. Phys. Commun. **267**, 108033 (2021)
[35] H. Yan, R. Liu, S. Li, Y.A. Zhang, W. Xiao, B. Xue, B. Xiong, X. Li, Z. Li, Materials **16**, 7581 (2023)
[36] S. Guo, C. Ng, L. Jian, C.T. Liu, J. Appl. Phys. **109**, 103505 (2011)
[37] B. Vishwanadh, N. Sarkar, S. Gangil, S. Singh, R. Tewari, G.K. Dey, S. Banerjee, Scr. Mater. **124**, 146 (2016)
[38] Z.F. Hou, Solid State Commun. **150**, 1874 (2010)
[39] J. Xu, Y. Lu, Y. Shen, P. Li, Y. Zhang, Mater. Today Commun. **31**, 103795 (2022)
[40] Y.T. Li, H.G. Fu, K.M. Wang, X.J. Yang, X.Y. Guo, J. Lin, Mater. Today Commun. **33**, 104869 (2022)
[41] F. Tasnádi, M. Odén, I.A. Abrikosov, Phys. Rev. B **85**, 144112 (2012)
[42] X. Song, X. Fu, M. Wang, Int. J. Mech. Sci. **243**, 108045 (2023)
[43] H.B. Shao, Y.C. Huang, Y. Liu, X.W. Ren, Z.B. Xiao, J. Mater. Res. Technol. **10**, 840 (2021)
[44] S.F. Pugh, Lond. Edinb. Phil. Mag. **45**, 823 (1954)
[45] L. Wang, J. Ding, S. Chen, K. Jin, Q. Zhang, J. Cui, B. Wang, B. Chen, T. Li, Y. Ren, S. Zheng, K. Ming, W. Lu, J. Hou, G. Sha, J. Liang, L. Wang, Y. Xue, E. Ma, Nat. Mater. **22**, 950 (2023)